A   Light scattering and its dependency on wavelength.

Scattering is a physical process where light is redirected in various directions upon encountering microscopic constituents of materials—such as atoms, molecules, or minute granules—that interfere with its path. When an electromagnetic wave encounters such a particle, it causes the electrons orbiting within the particle's molecules to oscillate at the same frequency as the incident wave's electric field [17]. This fluctuation acts as a source of electromagnetic radiation, which is the basis for the phenomenon of light scattering.

The scattering of light is dependent on the wavelength, which is observable in everyday phenomena, such as the pronounced scattering of red light by human skin when illuminated with a white flashlight, as shown in Fig. 12. The dependency can be understood through Mie scattering theory [27]. Mie theory describes the elastic scattering of electromagnetic radiation by spherical particles, taking into account the size of the particles relative to the wavelength of light. When considering a material as an ensemble of spherical

Fig. 12: Scattering of red light by a thumb illuminated with a white flashlight.

particles embedded in a homogeneous medium, Mie theory enables the derivation of analytical expressions for the material's scattering parameters: the phase function $p(\theta)$, the total scattering coefficient σ_s, and the total extinction coefficient σ_t [13]. All of these parameters are expressed as functions of the wavelength in vacuum together with the size of the spherical particles and the refractive indices of the particles and the embedding medium. We summarize the notation used in this paper in Tab. 3.

Assuming that only a single type of particles with the same radius and index of refraction are dispersed in the dispersing medium, the phase function of Mie theory, which specifies the normalized distribution of the scattered light for the bulk material, can be expressed as:

$$p(\theta) = \frac{|S_1(\theta)|^2 + |S_2(\theta)|^2}{4\pi K},\tag{8}$$

which is expressed with two scattering intensity functions of scattering angle θ:

$$S_1(\theta) = \sum_{i=1}^{\infty} \frac{2i+1}{i(i+1)} \left(a_i \pi_i(\cos\theta) + b_i \tau_i(\cos\theta)\right),\tag{9}$$

$$S_2(\theta) = \sum_{i=1}^{\infty} \frac{2i+1}{i(i+1)} \left(b_i \pi_i(\cos\theta) + a_i \tau_i(\cos\theta)\right),\tag{10}$$

and the scattering coefficient function:

$$K = \sum_{i=1}^{\infty} (2i+1) \left(|a_i|^2 + |b_i|^2\right).\tag{11}$$

Table 3: Notation used in the theory section.

Symbol	Description	Units
λ	Wavelength of light in vacuum	m
α	Spherical particle radius	m
n_{sph}	Complex index of refraction of spherical particles	—
n_{med}	Complex index of refraction of dispersing medium	—
C_s	Scattering cross-section coefficient of spherical particles	m^2
C_a	Absorption cross-section coefficient of spherical particles	m^2
C_t	Extinction cross-section coefficient of spherical particles	m^2
σ_s	Scattering coefficient of bulk material	m^{-1}
σ_s'	Reduced scattering coefficient of bulk material	m^{-1}
σ_a	Absorption coefficient of bulk material	m^{-1}
σ_t	Extinction coefficient of bulk material	m^{-1}
p	Phase function of the bulk material	sr^{-1}
$L(\mathbf{x}, \boldsymbol{\omega})$	Radiance at position $\mathbf{x}$ from direction $\boldsymbol{\omega}$	$\mathrm{Wm}^{-2}\mathrm{sr}^{-1}$
$R_f(r)$	Diffuse reflectance profile value at r	m^{-2}
A	Internal reflection coefficient	—

In Eq. (9) and Eq. (10), the functions π_n and τ_n are related to the Legendre polynomials P_n as follows:

$$\pi_n(\mu) = \frac{dP_n(\mu)}{d\mu}, \tag{12}$$

$$\tau_n(\mu) = \mu\pi_n(\mu) - (1 - \mu^2)\frac{d\pi_n(\mu)}{d\mu}. \tag{13}$$

a_i and b_i are the scattering functions, represented by:

$$a_i = \frac{n_{\mathrm{med}}\psi_i'(\xi)\psi_i(\kappa) - n_{\mathrm{sph}}\psi_i'(\kappa)\psi_i(\xi)}{n_{\mathrm{med}}\psi_i'(\xi)\zeta_i(\kappa) - n_{\mathrm{sph}}\zeta_i'(\kappa)\psi_i(\xi)}, \tag{14}$$

$$b_i = \frac{n_{\mathrm{sph}}\psi_i'(\xi)\psi_i(\kappa) - n_{\mathrm{med}}\psi_i'(\kappa)\psi_i(\xi)}{n_{\mathrm{sph}}\psi_i'(\xi)\zeta_i(\kappa) - n_{\mathrm{med}}\zeta_i'(\kappa)\psi_i(\xi)}, \tag{15}$$

where n_{med} and n_{sph} are the refractive indices of the dispersing medium and spherical particles, κ and ξ are the size parameter incorporating the ratio between the radius of the spherical particle α and the wavelength of light in vacuum λ:

$$\kappa = 2\pi\, n_{\mathrm{med}}\, \frac{\alpha}{\lambda}, \quad \xi = 2\pi\, n_{\mathrm{sph}}\, \frac{\alpha}{\lambda}, \tag{16}$$

and ψ and ζ denote Bessel functions of the second kind. Now, it is clear that all of the scattering intensity, coefficient, and phase functions depend on the wavelength λ, and the refractive indices n_{med} and n_{sph}, which are also dependent on λ.

The cross-section coefficients for scattering, absorption, and extinction are denoted by C_s, C_t, and C_a, respectively. They are calculated as follows:

$$C_s = \frac{\lambda^2 e^{-2\mathrm{Im}(\kappa)} K}{2\pi\gamma |n_{\mathrm{med}}|^2}, \tag{17}$$

$$C_t = 4\pi r^2 \mathrm{Re}\left(\frac{S(0)}{\kappa^2}\right), \tag{18}$$

$$C_a = C_t - C_s, \tag{19}$$

where

$$\gamma = \frac{2\left(1 + (a-1)e^a\right)}{a^2}, \quad a = 2\mathrm{Im}(\kappa), \tag{20}$$

and $S(0) = S_1(0) = S_2(0)$ is the amplitude in the forward direction of the scattered light. The absorption coefficient of the dispersing medium $\sigma_{a,\mathrm{med}}$ expressed as a function of the imaginary part of the complex index of refraction of medium n_{med}^* and wavelength, is required:

$$\sigma_{a,\mathrm{med}} = \frac{4\pi \mathrm{Im}(n_{\mathrm{med}}^*)}{\lambda}. \tag{21}$$

Consequently, σ_s, σ_t, and σ_a, the absorption coefficients of bulk material, are expressed as:

$$\sigma_s = C_s r^{-3} D, \tag{22}$$

$$\sigma_t = C_t r^{-3} D + \sigma_{a,\mathrm{med}}, \tag{23}$$

$$\sigma_a = \sigma_t - \sigma_s, \tag{24}$$

where D represents the density parameter, equivalent to the volume fraction of spherical particles in a unit volume of the bulk material.

The correlation between spectral scattering and the physical properties of materials is profound. Different materials have unique scattering properties due to their distinct σ_s, σ_t, σ_a, and the phase function p along side the incident light with wavelength λ, allowing for material-specific spectral signatures. This unique relationship is a cornerstone in our approach to material classification through spectral subsurface scattering imaging.

B   GRISM

Grism for spectral dispersion. Spectral dispersion for multispectral imaging has traditionally relied on optical prisms [2]. Yet, prism-based systems encounter inherent refractive distortions that challenge accurately capturing scattering kernels. Moreover, the refracted light paths necessitate an angled camera setup, complicating the focusing process. Ensuring high resolution in the spectral axis with strong dispersion necessitates a thicker prism, which will even deteriorate those problems. To circumvent these limitations, we combined a transmissive

diffraction grating with a prism, creating a grism. A grism is a combination of a prism with a grating to spectrally disperse and refract incoming light. When light from the scene passes through the diffraction grating first, it splits the light into its spectral components, which are then refracted by the prism. The behavior of light through the grating is governed by the grating equation:

$$m\lambda = d(\sin(\theta_m) - \sin(\theta_i)), \tag{25}$$

where m denotes the diffraction order, λ the wavelength of light, d the grating's groove spacing, θ_m the angle of the diffracted beam, and θ_i the angle of incidence relative to the grating's normal. Given that the prism is placed after the grating, the diffracted light enters the prism at an angle θ_m and refracts at an angle θ_r. Then, Snell's law, which describes this refraction, is given by:

$$n_1 \sin(\theta_m) = n_2 \sin(\theta_r), \tag{26}$$

where n_1 and n_2 are the refractive indices of air and the prism, respectively. For a right-angle prism with an apex angle of θ_p, if the refracted angle θ_r equals to θ_p, then the light will exit the prism perpendicularly. By searching the proper combination of the prism's apex angle θ_p and the grating's groove density d, we can engineer the grism to direct the first-order diffraction ($m = 1$) along the incoming light's path as shown in Fig. 5. Our configuration uses a right-angle prism with an apex angle of 30° and a diffraction grating with 300 lines per millimeter.

C   Justification of the single-shot technique

In this section, we aim to present the details of Sec. 4.1. We demonstrate the feasibility of the single-shot approach by showing the comparable optimization results obtained from our simulated single-shot approach against those derived from multishot $\mathcal{S}^4$ imaging. We employed the Farrell model, Eq. (2), as the physics model to be fitted from the spectral scattering data derived through the two $\mathcal{S}^4$ approach. This process involved a comparison between two models, one of them was optimized using multishot $\mathcal{S}^4$ images, and another one was optimized using single-shot $\mathcal{S}^4$ images simulated from the multishot images.

Utilizing the multishot imaging setup, we initially compiled a dataset of 11 materials—namely ceramic, egg, cotton, foam, milk, copy paper, coated paper, toilet paper, plastic, rubber, and wet wipe. Given the assumption that the measured kernel $k_m(x, y, i)$ is symmetric along the x and y axes, the diffuse reflectance in the i-th channel of multispectral subsurface scattering can be reformulated by a coordinate transformation as follows:

$$R_{f,d}^i(r) = k_m(r, i), \quad \text{where} \quad r = \sqrt{x^2 + y^2}. \tag{27}$$

Here, we assume that the origin of the kernel, where $r = 0, (x, y) = 0$, is the center point of the kernel. We extracted the diffuse reflectance $R_{f,d}$ at each channel

along with the distance from the center point of illumination. We averaged the scattering kernel over rotations around r to mitigate noise.

As a first optimization, we fitted the Farrell model to the extracted multi-spectral diffuse reflectance from the multishot images. The Farrell model defined for the optimization could be expressed as:

$$R_{f,m}(r, \sigma'_s, \sigma_a, A, S, C) = S \times R_f(r, \sigma'_s, \sigma_a, A) + C, \tag{28}$$

where S is the scaling factor accounting for the normalization of the captured data, and C is the offset value for pixel values on the background. Each optimization was performed by minimizing the following loss functions for $i - th$ channel:

$$\min_{\substack{\sigma'_s(i), \sigma_a(i), \\ A(i), S(i), C(i)}} \left\| R^i_{f,d}(r) - R_{f,m1}(r, \sigma'_s(i), \sigma_a(i), A(i), S(i), C(i)) \right\|^2_2. \tag{29}$$

As a second optimization, we simulated single-shot $\mathcal{S}^4$ images using the diffuse reflectance from multishot data and optimized the Farrell model with the simulated images.

$$\min_{\sigma'_s, \sigma_a, A, S, C} \left\| P(R_{f,d}) - P(R_{f,m2}(\sigma'_s, \sigma_a, A, S, C)) \right\|^2_F. \tag{30}$$

Here, as illustrated in Fig. 13, P is an operator that simulates single-shot $\mathcal{S}^4$ images from the diffuse reflectance and can be illustrated as:

$$P(R_{f,m}) = \sum_{i=1}^{16} \tilde{R}^i_{f,m}(x - s \times i, y), \quad \text{where} \quad \tilde{R}^i_{f,m}(x, y) = R^i_{f,m}(\sqrt{x^2 + y^2}). \tag{31}$$

Here s is a dispersion step size for each channel.

After finishing the optimization process, we computed the distance between the diffuse reflectances from the measurements and the optimized Farrell models. The distance was computed as:

$$d(R_{f,d}, R_{f,m}) = \sqrt{\sum_{i=1}^{16} \left\| R^i_{f,d} - R^i_{f,m} \right\|^2_2} \Big/ \sqrt{\sum_{i=1}^{16} \left\| R^i_{f,d} + R^i_{f,m} \right\|^2_2}. \tag{32}$$

The comparative analysis of the distance is illustrated in Fig. 6. It is important to note that $d(R_{f,d}, R_{f,m1})$ represents the minimum achievable distance between $R_{f,d}$ and $R_{f,m2}$. Observing the results, we find that $d(R_{f,d}, R_{f,m2})$ values are sufficiently small and exhibit a comparable scale to $d(R_{f,d}, R_{f,m1})$ across all materials, despite the complexity introduced by the image dispersion operation P. Specifically, $d(R_{f,d}, R_{f,m2})$ values
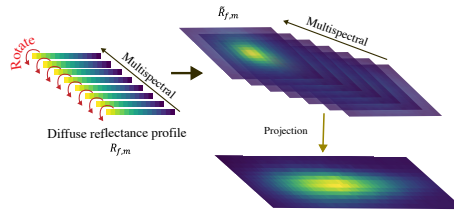
Fig. 13: Simulation of single-shot image

range from being only 1 to 2 times larger than $d(R_{f,d}, R_{f,m1})$. This proximity in values leads us to conclude that our single-shot $\mathcal{S}^4$ imaging method is capable of accurately representing the diffusive reflectance model, thereby encapsulating the unique optical properties of the materials under the measurements.

Anisotropic scattering. This paper would benefit from a discussion of anisotropic scattering, seen in biological tissues, crystals and minerals. Our dataset didn't include such materials; so our analysis assumed an isotropic scattering and extracted the scattering profile by averaging the scattering kernel over rotations around the center of illumination and fit a single scattering profile. However, it is possible to fit an anisotropic case by adding one more parameter for fitting, which is the anisotropy coefficient g included in the reduced scattering coefficient $\sigma'_s = (1 - g)\sigma_s$, where σ'_s is scattering coefficient. The g is a varying parameter based on the angle from the illumination center.

D   Spectral variation of scattering kernel shape for material classification

Our $\mathcal{S}^4$ imaging method captures two key physical properties of materials: (1) the spectral reflectance, indicated by the variations in the intensity values of the scattering kernel across the spectral domain, and (2) the variations in the spatial shape of the scattering kernel across the spectral domain. We can derive blurred information of the first property, spectral reflectance, as $\mathcal{S}^2$ measurement by integrating the projection of our single-shot $\mathcal{S}^4$ image along the row axis (spectral axis). In contrast, $\mathcal{S}^3$ measurements, as discussed in Sec. 4.2, offer only broadband scattering information. This is because projecting and integrating $\mathcal{S}^4$ image on the column axis aggregates the scattering kernel across all wavelengths, thereby omitting the detailed spectral variations of each scattering kernel. To rigorously assess the value of these spectral variations of scattering kernel, separate from reflectance information, we have executed a series of experiments detailed in this section.

D.1 $\mathcal{S}^2 + \mathcal{S}^3$ measurement.

To evaluate the significance of the scattering kernel's spectral variations in its shape, we conducted an initial experiment comparing the classification accuracy using $\mathcal{S}^2$, $\mathcal{S}^3$, and $\mathcal{S}^4$ against a combined $\mathcal{S}^2 + \mathcal{S}^3$ measurement. The $\mathcal{S}^2 + \mathcal{S}^3$ notation represents the concatenation of $\mathcal{S}^2$ and $\mathcal{S}^3$ vectors, resulting in a dimensionality of $2048 + 1200 = 3248$. Given that this concatenated vector could not reconstruct an image of the original $\mathcal{S}^4$ size as described in Sec. 4.2, we applied SVM and MLP classifiers, which accept vector inputs. Utilizing the same 25-class white material dataset as in the preceding experiment, we performed PCA to reduce the feature dimensionality to 375. The results, presented in Tab. 4, reveal that the combined $\mathcal{S}^2 + \mathcal{S}^3$ measurement achieves higher classification accuracy than either $\mathcal{S}^2$ or $\mathcal{S}^3$ alone, yet it falls marginally short of the $\mathcal{S}^4$ data

Table 4: Averaged classification accuracy from 3-fold cross-validation for $\mathcal{S}^2$, $\mathcal{S}^3$, $\mathcal{S}^2$ + $\mathcal{S}^3$, and $\mathcal{S}^4$ with different classifiers.

	$\mathcal{S}^2$	$\mathcal{S}^3$	$\mathcal{S}^2 + \mathcal{S}^3$	$\mathcal{S}^4$
SVM	40.53%	46.93%	49.33%	52.27%
MLP	41.33%	52.53%	53.06%	55.20%
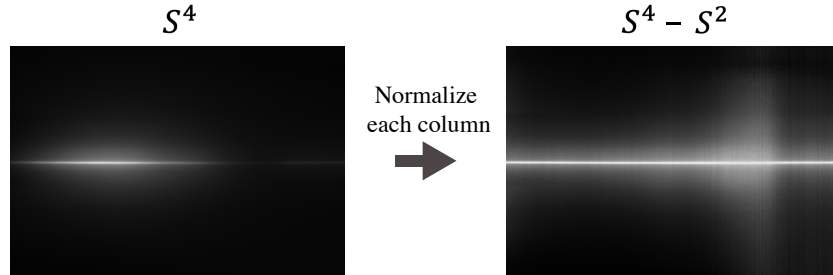
Fig. 14: Sample image (stone-jade) of $\mathcal{S}^4$ and $\mathcal{S}^4 - \mathcal{S}^2$ measurements. $\mathcal{S}^4 - \mathcal{S}^2$ data can be derived by normalizing each column of $\mathcal{S}^4$ image, solely encoding variation of scattering kernel shape in spectral axis.

accuracy. The superiority of $\mathcal{S}^4$ beyond $\mathcal{S}^2$ + $\mathcal{S}^3$ indicates the importance of the detailed spectral variations of scattering kernel separate from the spectral reflectance information for material classification.

D.2 $\mathcal{S}^4 - \mathcal{S}^2$ measurements

The second experiment was aimed explicitly at ascertaining the informativeness of spectral variation in the shape of the scattering kernel. We derived $\mathcal{S}^4 - \mathcal{S}^2$ measurements by normalizing each column within the $\mathcal{S}^4$ image, as shown in Fig. 14, thus isolating the spectral subsurface scattering information from the spectral reflectance. As indicated in Tab. 5, the $\mathcal{S}^4 - \mathcal{S}^2$ data outperformed $\mathcal{S}^3$ in terms of classification accuracy. This result underscores the value of integrating spectral shape variations of the scattering kernel into the classification process, providing an enhancement over solely broadband scattering data.

E   Ablation study

E.1   Search for the most informative spectral bands.

To identify the most informative spectral bands for material classification, we conducted an ablation study. We cropped the $\mathcal{S}^4$ and $\mathcal{S}^4 - \mathcal{S}^2$ images into 16 spectral bands, each representing a different wavelength range. We then performed classification using each of the 16 spectral bands with the same CNN model and compared the classification accuracy. The results are presented in

Table 5: Averaged classification accuracy from 3-fold cross-validation for $\mathcal{S}^2$, $\mathcal{S}^3$, $\mathcal{S}^4$ $-\mathcal{S}^2$, and $\mathcal{S}^4$ with the best classifier for each measurement.

$\mathcal{S}^2$	$\mathcal{S}^3$	$\mathcal{S}^4 - \mathcal{S}^2$	$\mathcal{S}^4$
41.33% (MLP)	54.13% (CNN)	56.80% (CNN)	58.80% (CNN)
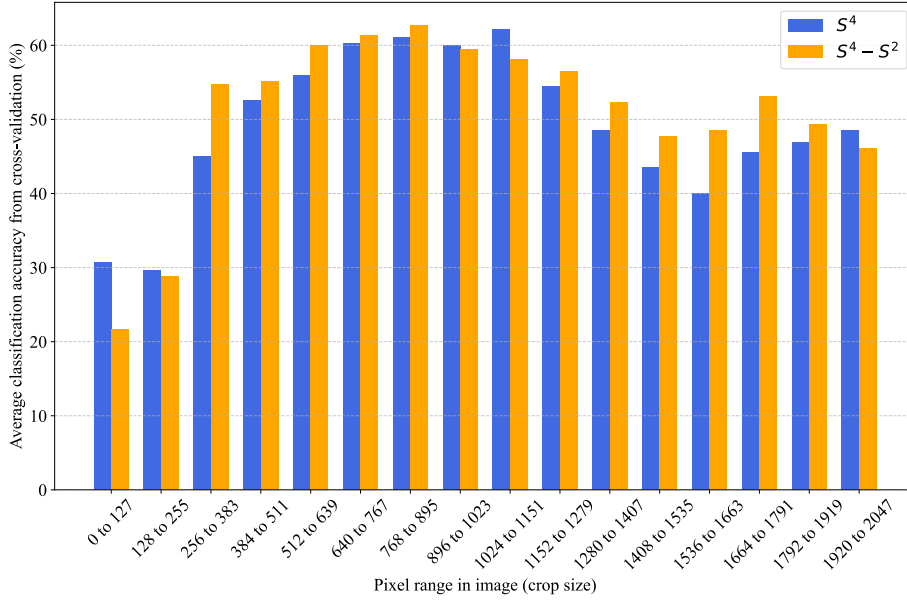
Fig. 15: Classification accuracy of each spectral band cropped from $\mathcal{S}^4$ and $\mathcal{S}^4 - \mathcal{S}^2$ images. The 6th to 9th bands (pixel location in the spectral axis: 640 to 1151) showed the highest classification accuracy for both measurements.

Fig. 15. Both measurements showed the increased classification accuracy 6th to 9th bands (pixel location in the spectral axis: 640 to 1151), which corresponds to the wavelength range of around 635nm to 791nm. This region has the highest signal values resulting from the spectrum of our light source and the sensitivity of our camera. The results indicate that beyond spectral information, higher SNR from brighter spectral bands is crucial for material classification with $\mathcal{S}^4$ imaging.

F   Additional results

(a) $\mathcal{S}^2$ with Ridge   (b) $\mathcal{S}^3$ with MLP   (c) $\mathcal{S}^4$ with CNN
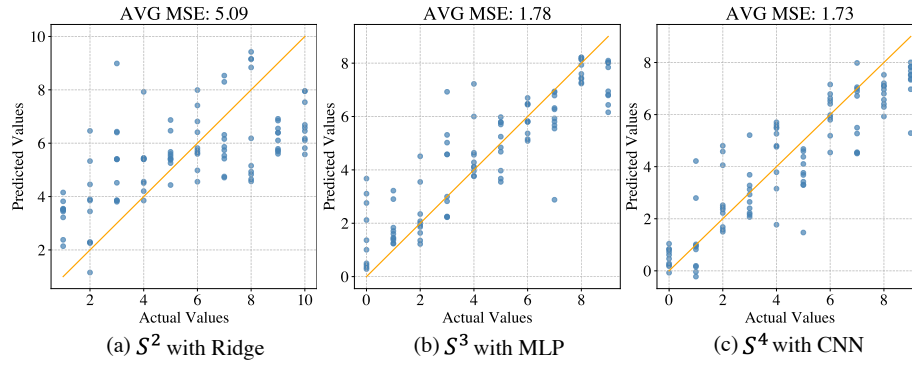
Fig. 16: Scattering plot of predicted and actual coffee concentrations from 2-fold cross-validation results for $\mathcal{S}^2$, $\mathcal{S}^3$, and $\mathcal{S}^4$ data with the best regression models.
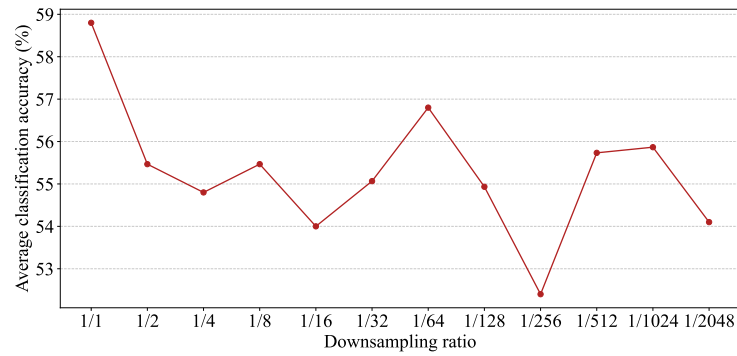
Fig. 17: Averaged white materials classification accuracies by downsampling the spectral axis in the single-shot images.